

1 **In-Situ Generation of CO_x-Free H₂ by Catalytic Ammonia Decomposition over**
2 **Ru-Al-Monoliths.**

3 Sabino Armenise^{a,b,c}*, Fernando Cazaña^b, Antonio Monzón^b, Enrique García-Bordejé^c

4 ^aUniversidad Politécnica Salesiana, Department of Biotechnology, Av. 12 Octubre,
5 170109, Quito, Ecuador.

6 ^bInstitute of Nanoscience of Aragon. Department of Chemical and Environmental
7 Engineering. University of Zaragoza. 50018, Zaragoza. Spain

8 ^cInstituto de Carboquímica (ICB-CSIC), Miguel Luesma Castán 4, 50018 Zaragoza,
9 Spain.

10

11 **Abstract**

12 Ru catalysts supported on alumina coated monoliths has been prepared employing three
13 different precursor, which are ruthenium chloride, ruthenium nitrosyl nitrate and
14 ruthenium acetyl acetonate, by an equilibrium adsorption method. The Ru particle sizes
15 could be controlled varying the metal precursor salt. Among the prepared catalysts, Ru
16 catalyst prepared from nitrosyl nitrate exhibited the highest activity which is
17 concomitant to the largest mean Ru particle size of 3.5 nm. The values of the apparent
18 activation energy calculated from the Arrhenius equation are according to the Temkin-
19 Phyzev model, indicating that the recombinative desorption of N ad-atoms is the rate-
20 determining step of the reaction. However, the ratio between the kinetic orders with
21 respect to ammonia and hydrogen ($-\alpha/\beta$), is not in agreement to the valued predict by
22 Temkin formalism. This fact could be related to the different operational conditions
23 used during the reaction, and/or catalyst nature, but not to any change on the controlling
24 step of the reaction.

25 **Keywords:** Structured Reactors; Ru-Catalyst; Ammonia Decomposition; Kinetics;
26 CO_x-Free; Nanoparticle.

* Corresponding author. Tel.: + 593 994787533; Email: sarmenise@ups.edu.ec

27

28 **1. Introduction**

29 Hydrogen combined with PEM fuel cells have attracted great interest recently as
30 substitute of fossil fuels in locomotion and other fields. However, hydrogen storage and
31 transportation involves great technical challenges to overcome. Its low energy per
32 volume unit, along with its flammability are factors which make difficult its storage as
33 gas at normal pressure [1]. Because of that, several technologies for hydrogen storage
34 have been proposed. These include storage at high pressures, either in liquid form or
35 adsorbed in a solid [2,3]. However, liquid H₂ requires high energy consumption and
36 expensive leak-free tanks. A more interesting option is the chemical storage in form of
37 easily storable and with high hydrogen content compounds, such as light hydrocarbons
38 or ammonia. These compounds must be decomposed in-situ to release a hydrogen
39 stream to feed the fuel cell. Recently, the production of hydrogen from the
40 decomposition of light hydrocarbons as methane, ethane or ethanol has attracted a great
41 researching interest [4]. Nevertheless, all these processes have the inherent drawback of
42 producing CO_x along with the H₂ stream. CO_x acts as poisons for PEM fuel cells, even
43 at concentrations as low as a few ppm [5]. Therefore, systems based on hydrocarbons
44 decomposition must include a series of purification steps, like desulfurization, water gas
45 shift, methanation, and preferential oxidation to reduce CO_x levels in the reformer outlet
46 gas. Ammonia, on the other hand, produces a CO_x-free stream of hydrogen, and
47 unconverted ammonia can be easily reduced to safe levels in one-step adsorption. In
48 addition, ammonia has a high H₂ content (17.7% wt) and can be stored in liquid form at
49 mild conditions (room temperature and 6 atms). For the whole process of H₂ storage as
50 NH₃ to be environmentally sustainable, the H₂ and the energy required for synthesis and
51 decomposition process should be produced using renewable energies. On the other

52 hand, the energy needed for decomposition of NH_3 could be generated using a small
53 percentage of the energy stored in NH_3 . This percentage will be minimized if a catalyst
54 active at the lowest temperature as possible is used and obtaining a high-purity H_2
55 stream. All this characteristic make more economically feasible the hydrogen
56 production from ammonia than others career [6].

57 In the last years, ammonia decomposition reaction has been extensively studied for H_2
58 generation, including the catalytic active phase to the reactor structure and design [7].
59 Yin et al., reported that ruthenium exhibits the highest TOF in ammonia decomposition
60 [8]. Therefore, research has been focused on ruthenium supported on different carriers,
61 such as alumina [9–11] or others transition metal oxides like MgO [12], activated
62 carbon [13,14], or carbon nanotubes/nanofibers [15–18]. Bimetallic combinations of
63 transition metals (MoCo) have also proved to be active enough to replace ruthenium
64 catalyst [19–23]. From the point of view of reactor design, microstructured reactors
65 have improved the performance of the conventional packed bed reactors [24–27].

66 One century after the development of Habber-Bosch process, ammonia mechanism still
67 being investigated by several authors to obtain more precise information about reaction
68 mechanism and to explain the wide range differences observed on the kinetic
69 parameters.

70 The mechanism of ammonia decomposition reaction has been grouped in two limiting
71 cases: (i) effect of ammonia concentration, (ii) effect of hydrogen concentration.

72 At low ammonia concentrations and low temperatures [28,29], the reaction rate shows
73 non-dependence with respect to ammonia. However, at high temperatures the reaction
74 becomes first-order with respect to ammonia [30,31]. These transition temperature has
75 been investigated by Tamaru [32] and Chellappa [33], and explained by a change of
76 reaction mechanism. At temperature below 650 K the recombinative desorption of N-

77 adsorbed species is the rate-determining step (RDS), while at high temperature (< 750
78 K), cleavage of N-H bond on NH₃ adsorbed species is the RDS [30,31].

79 At high hydrogen partial pressure and low temperature, the reaction is found to be
80 inhibited by hydrogen [33]. In these operational conditions the reaction is explained by
81 Temkin-Phyzev mechanism [32,34]. This reaction mechanism assumes that both
82 recombinative desorption of N-species and N-H cleavage are the RDS. Inhibitory
83 effects of hydrogen could be associated to the re-hydrogenation of N-species adsorbed
84 or by blocking the active sites by competitive adsorption, where ammonia
85 decomposition takes place. At high temperature and low hydrogen partial pressure (low
86 conversion), Temkin-Phyzev model could be re-written as Tamaru's model [32,35].

87 This work is a new contribution of our group to the study of the ammonia
88 decomposition reaction, using nickel catalysts supported on honeycomb monoliths
89 prepared by electrostatic adsorption structured reactors [27]. Herein, our aim is to
90 investigate the performance of Ru-based reactors, and , to obtain uniformly dispersed
91 Ru nanoparticles in alumina coated monoliths. To this end, different Ru precursors were
92 tested. The catalysts after reduction were characterized by STEM, TPR and XPS and
93 tested in the decomposition of pure ammonia. Also, a kinetic study is carried out in
94 order to determine the effect of precursor synthesis on the main apparent kinetic
95 parameters: activation energy and reaction orders.

96 **2. Experimental**

97 2.1. Materials and Catalyst Preparation

98 Cordierite monoliths were carved out from blocks supplied by Corning (400 cpsi) to the
99 desired dimensions (65 mm long, 10 mm diameter, ca. 2,4 g). These monoliths were
100 impregnated with alumina by a dip coating method, as described elsewhere [27]. A sol-
101 gel was prepared by mixing pseudoboehmite (AlOOH pural, from Sasol), 0.3 M nitric

102 acid and urea, in 2:5:1 proportion. After stirring for 24h, monoliths were immersed in
103 the mixture until ensuring the absence of air bubbles in the channels. Following up, the
104 excess of liquid was removed with pressurized air and the monoliths were dried for 24
105 hours at room temperature while rotating around its axis. Later, the monoliths were
106 thermally treatment under 100 ml/min air flow for 2 hours at 873 K, at a heating rate of
107 1 K/min.

108 The deposition of ruthenium nanoparticles was carried out by equilibrium adsorption or
109 electrostatic adsorption method [36]. In this method, the ions of precursor in solution
110 are bound by electrostatic forces to the sites of opposite charge at support surface. Three
111 different Ru precursors were used. Ruthenium Chloride ($\text{RuCl}_3 \cdot x\text{H}_2\text{O}$) dissolved in 10
112 ml of 0.1M HCl, ruthenium nitrosyl nitrate ($\text{Ru}(\text{NO}_3)_3(\text{NO})$) dissolved in 10 ml of
113 distilled water and ruthenium acetyl acetonate ($\text{RuC}_{15}\text{H}_{21}\text{O}_6$) dissolved in 10 ml of
114 toluene. The weight of ruthenium in solution was calculated on the basis of a nominal
115 weight percentage of 5 wt% with respect to alumina coating. The alumina coated
116 monoliths were fitted to a vial with the impregnating solution and rotated continuously
117 perpendicular to its axis for 24 hours. In this process, the liquid with the precursor flows
118 through the monoliths channels and it is concomitantly homogenized due to the rotating
119 movement. After this process, the liquid inside the channels was removed with
120 pressurized air and the monoliths were dried under rotation for 24 hours. Finally, they
121 were calcined in 100 ml/min of N_2 at 873 K during 2 h, using a heating rate of 1 K/min.
122 The monolith samples were denoted as Ru(Cl)/Al/M, Ru(NN)/Al/M and Ru(acac)/Al/M
123 for catalysts prepared from ruthenium chloride, ruthenium nitrosyl nitrate and
124 ruthenium acetyl acetonate, respectively.

125 Deposition of metal by electrostatic adsorption or ion-exchange it is useful way to
126 incorporate well-dispersed metal in different kinds of supports. This technique should

127 get a balance in the equilibrium between the charges on the surface of support, and the
128 charge of metal-ions in solution. For this reason, achieving a desired metal-loading it is
129 not a trivial problem, and it is necessary make successive impregnations by this
130 technique.

131 However, for supports like pellets, or other configurations where the layer thickness or
132 particle radius are bigger than few microns, metal-ions diffusion into the particle or
133 support may be difficult. For conventional catalyst supports, this will result in egg-shell-
134 type metal distributions. This kind of problems can be avoided choosing specific
135 complex-metal, which can lead to slow adsorption process [37].

136 During the first step of this work (no presented here), we analyze the effects of
137 successive metal deposition (specifically nickel metal) and enhanced the metal
138 adsorption by process in a vacuum system, to increase the weight/volume ratios. The
139 results obtained shows both process increase the metal loading, but with any positive
140 effect on the catalytic ammonia decomposition reaction may be related to lower
141 dispersion reached by the impregnation process.

142 The actual Ru content was analyzed by inductive coupled plasma optical emission
143 spectroscopy (ICP-OES) after digestion of the samples in lithium borohydride. In
144 addition, Ni catalyst was also prepared from a nickel nitrate solution as described
145 previously [23]. The actual Ni loading determined by ICP-OES was 15 wt%.

146 It is well-knew that the stability of the catalytic coating is closely related to adhesion
147 strength of alumina-washcoated on the monolith walls, and is a key step to be evaluated
148 to scale up this kind of catalyst to real use. The stability of the catalytic coatings were
149 measured by ultrasonication for 30 min and reported in previous work by our group
150 [38]. These results indicate that catalytic coating is properly attached to the walls.

151 Despite that case we had nanofibers deposited on alumina washcoated on monolith

152 reactor, the washcoated alumina was produced in the same way those presented in this
153 work, and then the result can be extrapolated.

154

155

156 2.2. Catalytic Testing

157 Catalyst reactivity system consists of a continuous-flow 15 mm i.d. quartz reactor inside
158 horizontal furnace with a temperature controller (Eurotherm). The monolithic nickel
159 catalyst was wrapped with quartz stripe and it was tightly fitted to the wall of the quartz
160 reactor to avoid channeling. Subsequently, the reactor was placed in the constant
161 temperature zone of the furnace. The reaction testing was carried out after catalyst
162 reduction in hydrogen atmosphere (100 ml/min H₂:N₂, 50:50) at 773 K for 1 h.
163 Catalysts were tested between 573 and 973 K using 100 ml/min of pure anhydrous
164 ammonia as feed gas. The outlet reaction gases were analyzed with an Agilent Micro
165 GC 3000A. H₂ and N₂ were analyzed in a molsieve column and ammonia in a Plot-Q
166 column. To ensure repeatability, 2–3 separate GC samples were taken and averaged for
167 each experimental data point, and analyses were typically within ±3% of each other.
168 The conversion was calculated taking into account the variations in the flow due to the
169 mole increase in the reaction.

170 2.3. Catalyst Characterization

171 The catalysts after reaction were tested by different techniques. Temperature
172 programme reduction (TPR) was carried out in a Micromeritics AutoChem II 2920. In
173 TPR experiments, the catalyst was heated in 50 ml/min (STP) of 10% H₂ in Ar up to
174 1273 K with a heating rate of 10 K/min.

175 XPS technique was used to measure the Ru oxidation state. The apparatus was an
176 ESCAPlus Omnicrom system equipped with a Mg K α radiation source to excite the

177 sample. Calibration of the instrument was done with Ag 3d_{5/2} line at 368.27eV. All
 178 measurements were performed under UHV, better than 10⁻¹⁰ Torr. Internal referencing
 179 of spectrometer energies was made using the dominating Al 2p peak of the support, at
 180 74.0 eV and corroborated with the C 1s signal at 284.4 eV. The curve fitting of the
 181 spectra was performed using CASA XPS software after applying a Shirley baseline.
 182 Catalyst particle size was studied by scanning transmission electron microscopy
 183 (STEM) using a FEI TECNAI F30 electron microscope equipped with Gatan Energy
 184 Filter and cold field emission gun (FEG) operated at 300 kV with 1.5 Å lattice
 185 resolution. TEM specimens were prepared by ultrasonic dispersion in ethanol of powder
 186 retrieved from the monoliths. A drop of the suspension was applied to a holey carbon
 187 support grid.

188 3. Results and Discussion

189 3.1 Textural and morphological characterization

190 Table 1 shows the textural properties of the prepared catalysts. All Ru catalysts exhibit
 191 similar textural properties and the surface area is comparable to that of the support (246
 192 m²/g). There are not significant differences between the Ru content deposited using the
 193 different salt precursors.

194 Table 1. Textural properties measured by N₂ physisorption and surface composition
 195 measured by XPS of Ru catalysts on alumina coated monoliths prepared from different
 196 precursors.

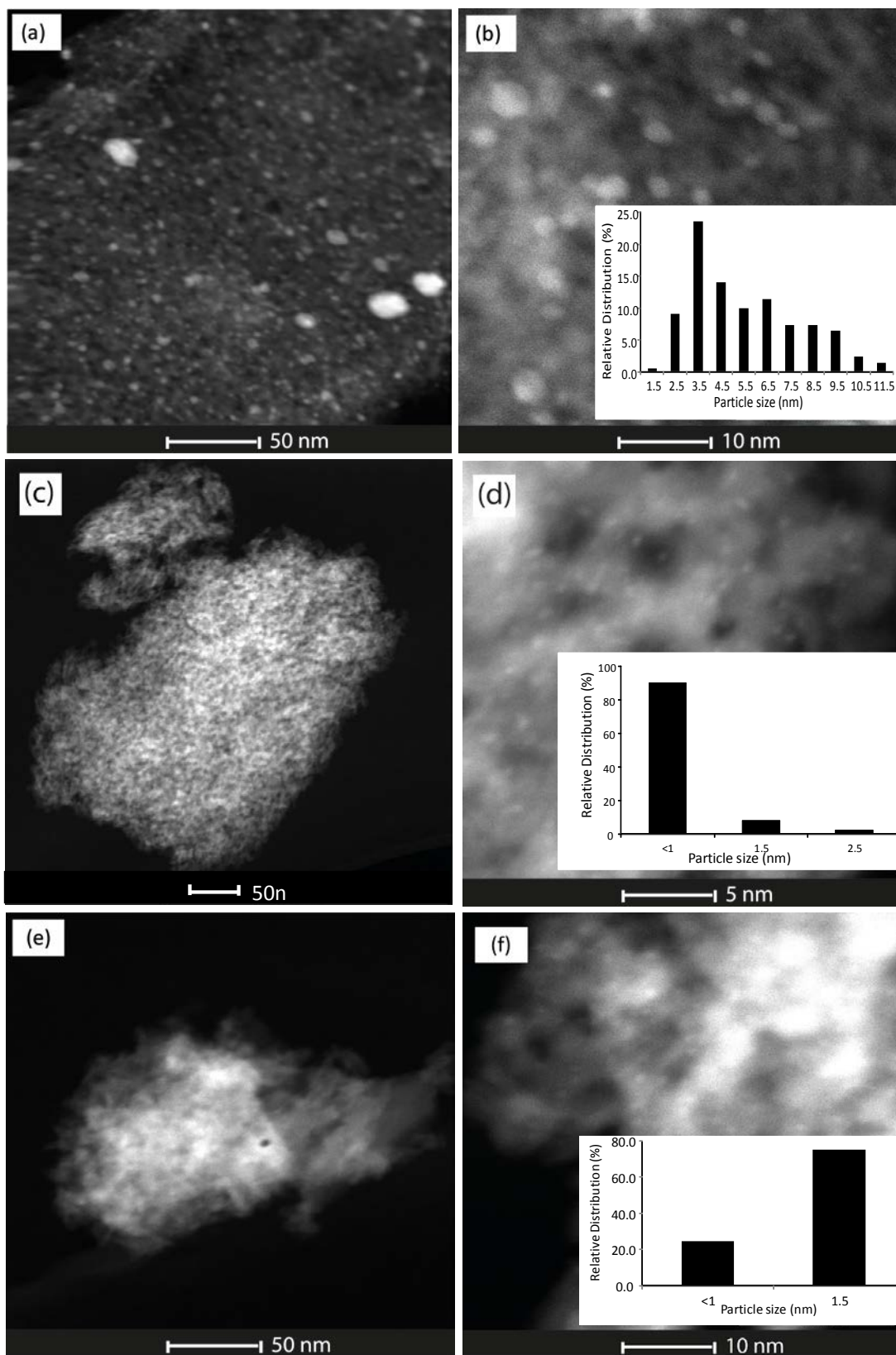
Catalyst	Ru/Al ¹ wt. %	Surface Area (m ² /g)	Pore diameter (nm)	Ru/Al ² wt. %	Ru ⁰ /Ru _{total} ² at. %
Ru(NN)/Al/M	3.0	238	6.0	6.7	69.1
Ru(Cl)/Al/M	3.6	215	6.0	6.4	5.7
Ru(acac)/Al/M	3.0	233	5.5	5.6	7.4

197 ¹Measured by ICP-OES

198 ²Measured by XPS

199

200 The ruthenium particle size was characterized by STEM. Fig. 1 shows representative
201 STEM images and particle size distribution (inset) for the several catalysts prepared.
202 For Ru(NN)/Al/M (Fig. 1a, and 1b) the particles are spherical with heterogeneous
203 distribution particle sizes, ranging between 1 and 10 nm with a mean size of 3.5 nm. On
204 the other hand, for Ru(Cl)/Al/M and Ru(acac)/Al/M (Fig. 1c to 1f) the particle size are
205 predominantly smaller than 1.5 nm, with a homogeneous distribution. The mean particle
206 size is subnanometric for Ru(Cl)/Al/M and 1.5 nm for Ru(acac)/Al/M.



207

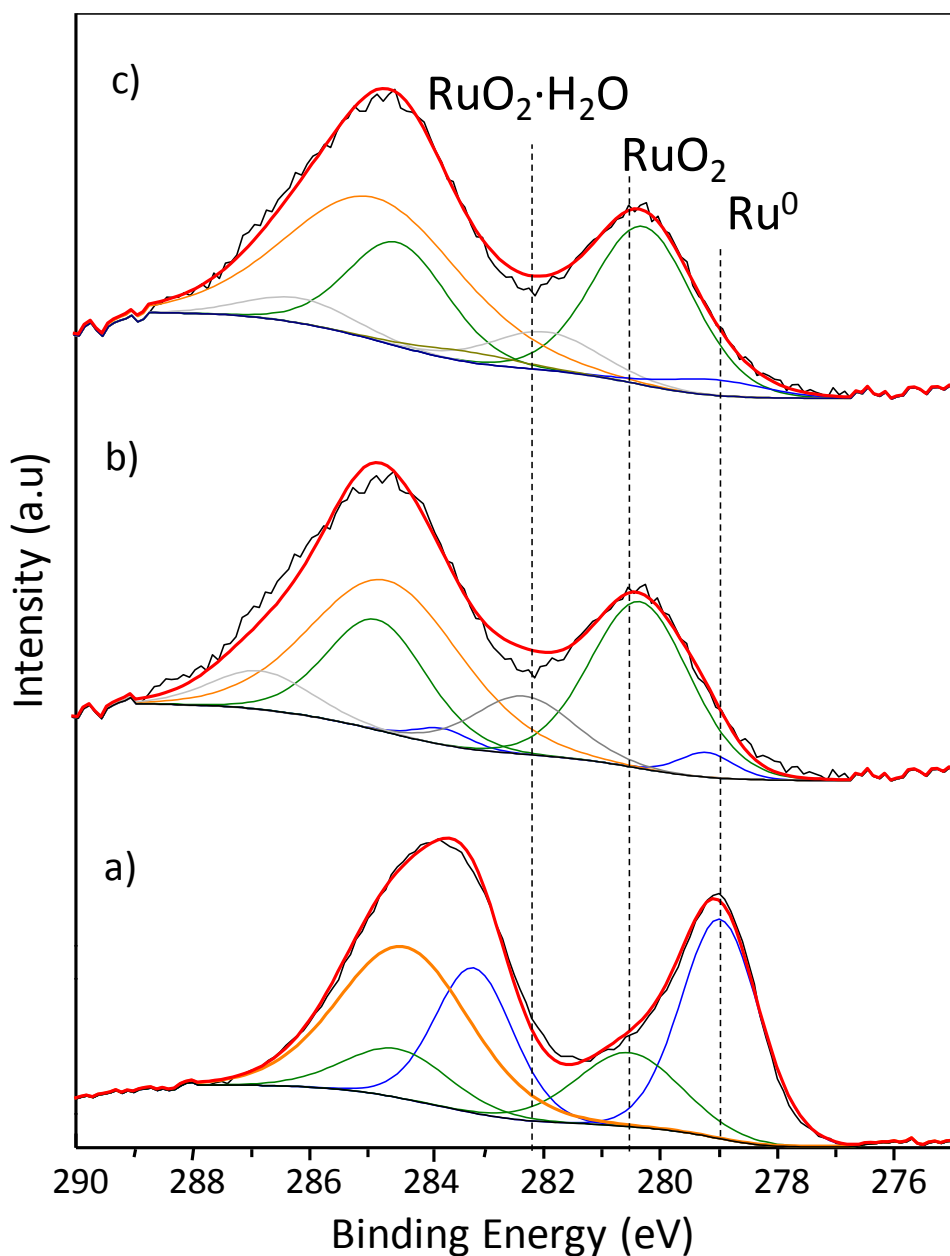
208 **Fig. 1.** Representative STEM images at two different magnifications and particle size
 209 distribution of catalysts used in reaction: (a,b) Ru(NN)/Al/M; (c,d) Ru(Cl)/Al/M y (e,f)
 210 Ru(acac)/Al/M.
 211

212 3.2. Ru oxidation state characterization

213 Fig. 2 shows the deconvolution of XPS Ru signal according to the literature
214 assignments [25-28]. In addition, the quantification of Ru/Al and $\text{Ru}^0/\text{Ru}_{(\text{total})}$ atomic
215 ratios determined by XPS are displayed in table 1. The Ru/Al ratio determined by XPS
216 is similar for all the catalysts synthesized and these ratios are around twice that those
217 determined by ICP. This result indicates that the surface of the alumina coating is
218 enriched by Ru.

219 In the deconvolution of Ru 3d XPS signal of Ru(NN)/Al/M (spectrum a of Fig. 2) only
220 the peaks at 279.1 eV and 280.5 eV are present, which are associated to Ru^0 and RuO_2
221 species [39–42], respectively. However, for the catalyst Ru(Cl)/Al/M and
222 Ru(acac)/Al/M, besides the peaks associated to Ru^0 and RuO_2 , is observed a new signal
223 centered at 282.3 eV, which can be ascribed to hydrated RuO_2 species [43].
224 Additionally, a peak centered at 284.4 eV has been observed in all the catalysts which is
225 attributed to carbon contamination.

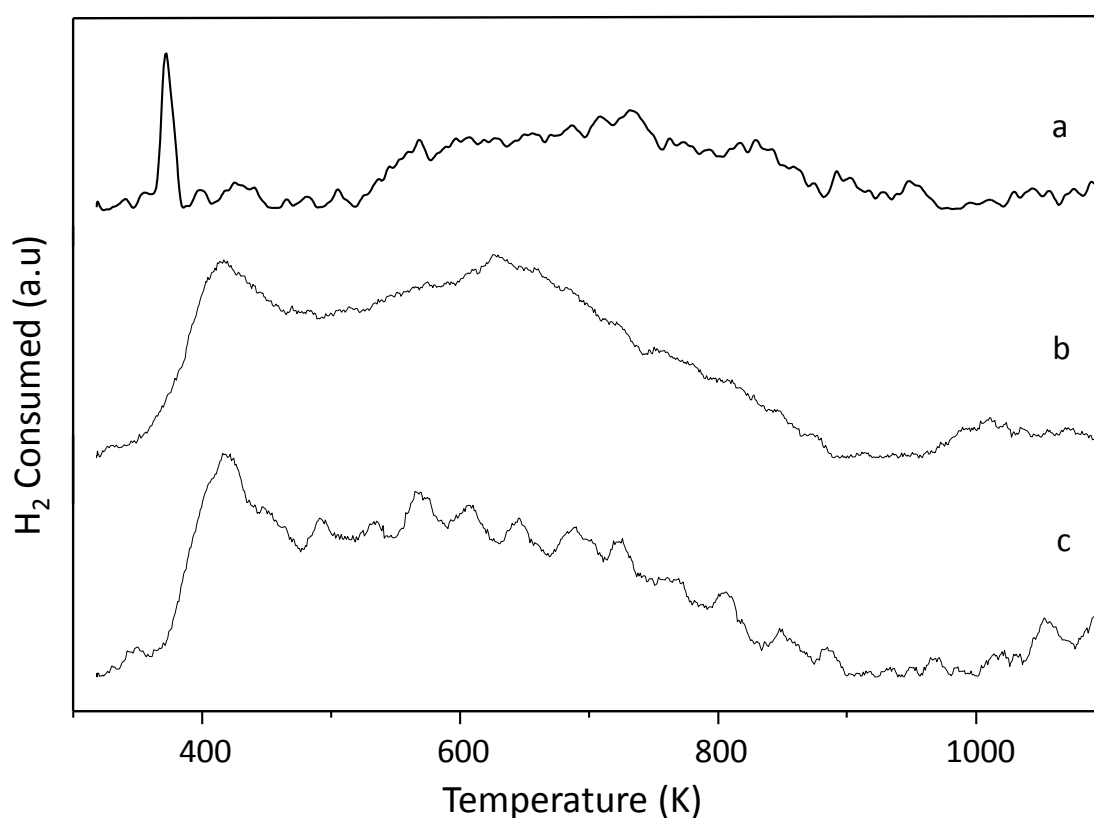
226 The catalysts Ru(Cl)/Al/M and Ru(acac)/Al/M show $\text{Ru}^0/\text{Ru}_{(\text{total})}$ ratios substantially
227 smaller than the catalyst Ru(NN)Al/M. In the XPS spectra of Ru(Cl)/Al/M, a signal at
228 198.5 eV was observed indicating the presence of chlorine ions. It is well known that
229 electronegative species such as chlorine can increase the oxidation state of metals
230 [44,45], which could explain the lower $\text{Ru}^0/\text{Ru}_{(\text{total})}$ ratios. However, the effect of
231 electron-withdrawing species cannot be invoked to explain the lower $\text{Ru}^0/\text{Ru}_{(\text{total})}$ ratios
232 of Ru(acac)/Al/M. Therefore, the most plausible explanation is that metal oxidation
233 state is governed by interaction with the support, which is particle-size dependent. Thus,
234 the smaller the Ru particles, the stronger is the metal support interaction, leading to
235 lower $\text{Ru}^0/\text{Ru}_{(\text{total})}$ ratios.



236
 237 **Fig. 2.** XP Spectra of 3d core level of ruthenium of the catalyst used in reaction: (a)
 238 Ru(NN)/Al/M; (b) Ru(Cl)/Al/M and (c) Ru(acac)/Al/M.

239
 240 The passivated catalysts after reaction were also studied by temperature programmed
 241 reduction (Fig. 3). The TPR profile of Ru(NN)/Al/M shows two peaks, one intense peak
 242 at low temperature (ca. 380 K) which can be attributed to surface oxidized large Ru
 243 nanoparticles and a broad peak at higher temperatures which can be attributed to
 244 oxidized smaller Ru particles, interacting strongly with the support. The other two
 245 catalysts, Ru(Cl)/Al/M and Ru(acac)/Al/M, exhibit similar TPR profiles with two

246 shoulders, one at ca.430 K and other in the range of 550-750 K which correspond to
247 RuO₂ particles with some kind of interaction with support. The peak showed at low
248 temperatures (380 K) is absent in these two latter catalysts, suggesting that the smaller
249 particles, present in these catalysts, have stronger interaction with the support. On the
250 other hand, the larger particles found for Ru(NN)/Al/M are oxidized only on the
251 outermost surface but the inner bulk metal remains in reduced state in agreement with
252 XPS results [21].

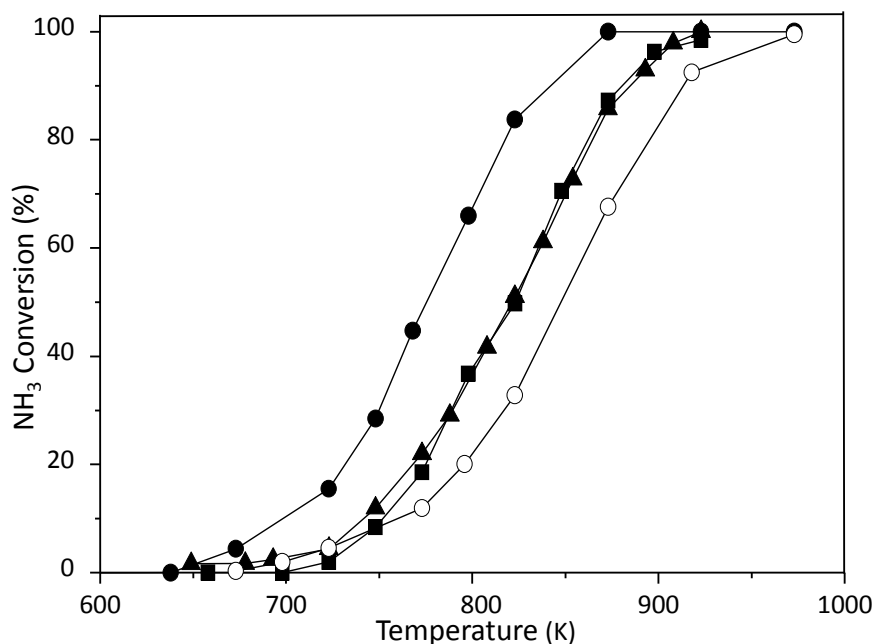


253
254 **Fig. 3.** TPR profile of catalysts passivated after reaction for Ru catalysts (a)
255 Ru(NN)/Al/M; (b) Ru(Cl)/Al/M and (c) Ru(acac)/Al/M.
256

257 3.3. Catalytic testing in NH₃ decomposition

258 Fig. 4 shows the NH₃ conversion vs. temperature plot for the Ru-based catalysts. This
259 figure also includes the curve obtained for the catalyst that contains a 15% Ni on
260 Alumina coated monolith. The preparation and characterisation of this Ni/Al/M catalyst
261 is reported in a previous publication [46]. All Ru-based catalyst exhibit higher

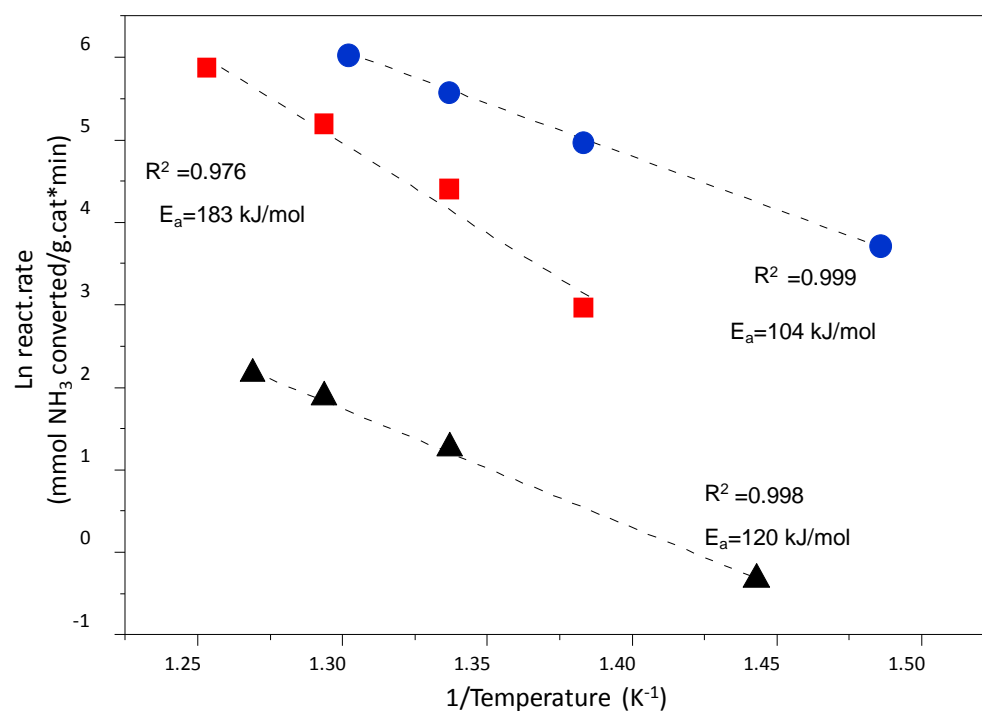
262 conversion than Ni-based catalyst although the metal loading is five-fold higher for the
263 later, ca. 3 and 15wt.%/Al₂O₃, respectively. Noticeably, the mean particle size of Ni
264 was larger than for Ru catalysts, 6 nm vs. 3.5 nm for Ru(NN)/Al/M. This seems to
265 indicate a larger intrinsic activity of Ru metal, in agreement with the literature [21].



266 **Fig. 4.** NH₃ conversion at steady state as a function of the reaction temperature for
267 different catalysts. (●) Ru(NN)/Al/M; (■) Ru(Cl)/Al/M; (▲) Ru(acac)/Al/M and (○)
268 Ni/Al₂O₃/Monolith. Conditions: 100 ml/min pure NH₃, space velocity: 35000 h⁻¹/g
269 Ni/Al₂O₃.

270
271 Comparing among Ru-based catalysts, the one prepared with nitrosyl nitrate
272 (Ru(NN)/Al/M) exhibits higher conversion, for all temperatures studied, than those
273 prepared with other precursors. Since the main difference between Ru(NN)/Al/M and
274 the other catalysts is the particle size, it is reasonable to think that this fact may be the
275 responsible of the different catalytic behaviour. Jacobsen and coll. reported that B₅-type
276 sites have the adequate geometry for the ammonia decomposition [47]. The number of
277 these sites decreases as the particle size diminishes. This fact has been experimentally
278 confirmed by several authors, who observed an increase of the turnover frequency as the
279 metal particle size increased [48–50]. Xu and cols. [51] reported that there was an
280 optimum Ru particle size of 2.2 nm that maximized turnover frequency. They also
281

282 found that the apparent activation energy increased from 79 kJ mol^{-1} to 122 kJ mol^{-1} as
 283 the mean Ru particle size decreased from 4.6 to 1.9 nm. The apparent activation
 284 energies of the different catalysts prepared were calculated from the Arrhenius equation
 285 (Fig. 5) at low conversion ($<10\%$), in order to operate into differential condition. The
 286 apparent activation energy for Ru(NN)/Al/M was 104 kJ mol^{-1} , which was smaller than
 287 those determined for Ru(acac)/Al/M and Ru(Cl)/Al/M, 120 kJ mol^{-1} and 183 kJ mol^{-1} ,
 288 respectively. It is possible that presence of chlorine ions may act as inhibitor in the
 289 catalyst prepared with ruthenium chloride, contributing to the lower conversion and
 290 higher apparent activation energy for this catalyst.



291
 292 **Fig. 5.** Arrhenius plot and estimation of the apparent activation energies for the Ru
 293 catalysts from different precursors. (●) Ru(NN)/Al/M; (■) Ru(Cl)/Al/M; (▲)
 294 Ru(acac)/Al/M.
 295

296 A long-term reaction was also evaluated to determine the stability of the Ru(NN)/Al/M
 297 catalyst (showing the best performance) after 15 h of reaction. The results show similar
 298 reaction profile for the same catalyst. However, a slight variation on the conversion was

299 measured (support information, Figure.S1). Considering the variation showed after long
300 reaction is around 5-7% less of measured during first run, it is possible to associate this
301 change to internal deviations of the analysis techniques and possible sintering effects.
302 However, thermal sintering of the metallic nanoparticles cannot be dismissed. This
303 phenomenon is strongly promoted by high operating temperatures. If the involved
304 mechanism is controlled by the diffusion of atoms through the support, the sintering rate
305 correlates to Tamman temperature, but if the diffusion of atoms occurs at the outermost
306 surface, depends on the Hütting temperature [52]. Both parameters are closely related to
307 the melting point of metal catalyst (2607 K). In our case, the reaction temperature
308 reached 100 K degree above the Hütting temperature ($T_{\text{Hütting}} = 0.3 \times T_{\text{melting}} = 780 \text{ K}$),
309 which could be induce some sintering effects.

310

311 3.4. Mass and Heat Transfer Consideration

312 Monolithic reactors have attracted a huge interest to support catalytic material for many
313 applications in the last decades. Ones of the most important advantages are low
314 pressure-drop and large geometrical surface area compared to traditional packed bed
315 reactor. However, taking into account that reactant must diffuse from gas-solid phase,
316 and flow developed inside the monolithic channel present characteristic, mass and heat
317 transfer limitation have been considered for many authors has an interesting topic to
318 analyses and avoid the reaction will be controlled by diffusion phenomena.

319 In this work, the possible problems of mass transfer were evaluated by performing
320 previous experiments at different linear velocities of the feed gas, keeping the spatial
321 velocity constant, in the operating range used (spatial time $1.827 \times 10^{-5} \text{ mol/g.min}$), any
322 significant differences in the conversion were observed when increasing the linear
323 velocity of the gas.

324 Otherwise, the restrictions due to internal diffusion were evaluated by the Weisz-Prater
325 criterion [53], assuming a particle size equivalent to 1/3 of the thickness of the layer of
326 product deposited in the monolith (the thickness of alumina coating deposited and
327 measured by EDX-SEM Mapping was $2.7\mu\text{m}$). In the conditions of operation studied in
328 this work, this criterion takes values lower than 0.1, indicating that the effects of
329 internal diffusion are not important.

330 Regarding the influence of the thermal effects, and the moderately endothermic
331 character (86 kJ/mol) of the reaction, in the operating conditions where the restrictions
332 of matter transfer are minimized, the calculation of the Anderson criterion and of Mears
333 [54,55], assuming as effective particle radius 1/3 of the thickness of the catalytic layer,
334 also confirming that the effects of heat transmission are negligible in the evaluation of
335 the catalytic activity and the kinetic parameters observed.

336 Given that the flow developed inside monolith channel is of laminar-type, the reacting
337 species must be transferred to from the gas stream to the monolith wall by molecular
338 diffusion. This fact linked to large values of the reaction rate may cause that mass
339 transfer phenomena will be the reaction controlling step. However, combining a proper
340 synthesis process, and tuning the specific reaction conditions it can be improved the
341 surface contact. Another way to enhance the contact surface area between gas and solid
342 phases is to induce turbulences inside the monolith channels, or to enhance axial
343 diffusion between them.

344 Additionally, other way to reach higher performance of these type of reactors is
345 achieving a closer interaction between gas-solid phase by modifying the rugosity of the
346 walls. Carbon nanofibers can form aggregates with high surface area, high mesopore
347 volumes and low tortuosity. Additionally, the possibility to manipulate diameter and
348 length as well as the bulk density of CNF, open an opportunity to tailor the porosity and

349 overcome tortuosity problems. This reduces or eliminates the internal diffusion
350 limitations by preventing concentration gradients inside the monolith channels. This
351 situation is very favorable for fast and highly exothermic gas-phase reactions, and for
352 sluggish liquid phase reactions because mass/heat transfer limitations are prevented
353 while keeping low pressure drop. In fact, the advantages of incorporating this kind of
354 materials has been investigated by our groups previously. The effect to anchor carbon
355 nanofibers (CNF) and N-doped carbon nanofibers (N-CNF) to the alumina washcoated
356 monolith for ammonia decomposition and other reactions have shown results very
357 promising [15,56]. Modify the surface channels by carbon or other nanomaterials open
358 a new possibility to take advantages of structured reactors and at the same time reduce
359 mass and heat transfer phenomena.

360

361 3.5. Kinetic Model

362 The development of an efficient reactor requires necessarily a depth understanding of
363 kinetic aspects. Many researches related to ammonia decomposition reaction have been
364 carried out under high vacuum condition and with model catalysts. These conditions are
365 not comparable to fuel cell systems fed by ammonia decomposition reaction where
366 usually high ammonia concentration, atmospheric pressure and high temperature have.

367 Regarding to ammonia decomposition kinetics, many authors have fitted the
368 experimental data using the Themkyn-Pyzhev model:

$$(-r_{NH_3}) = k \left[\left(\frac{P_{NH_3}^2}{P_{H_2}^3} \right)^m - \frac{P_{N_2}^2}{K_{eq}^2} \left(\frac{P_{H_2}^3}{P_{NH_3}^2} \right) \right] \quad (1)$$

369 Where m is a constant related to the non-uniformity surface, and the second term
370 corresponds to the contribution of the reversible equation (i.e. que driving force to the
371 equilibrium). According with the experimental conditions (673 K -1023 K), and to the

372 results previously reported [57], this term is virtually zero, indicating that the reaction is
373 not limited by equilibrium, and therefore this contribution can be neglected.

374 The Temkin-Pyzhev model may be rewrite to the power law rate expression:

$$(-r_{NH_3}) = k' P_{NH_3}^\alpha P_{H_2}^\beta \quad (2)$$

375 where k and k' follows an Arrhenius dependence with the temperature, [32,58,59] and α
376 and β are the kinetic orders with respect ammonia and hydrogen, respectively.

377 The kinetic parameters were calculated by non-linear multivariable regression using
378 Levenberg–Marquardt algorithm coupled to a Runge–Kutta–Fehlberg routine, using the
379 steady-state ammonia mass balance in plug-flow reactor, [57]:

$$(-r_{NH_3}) = \frac{dX_{NH_3}}{d(W_{cat}/F_{NH_3}^0)} \quad (3)$$

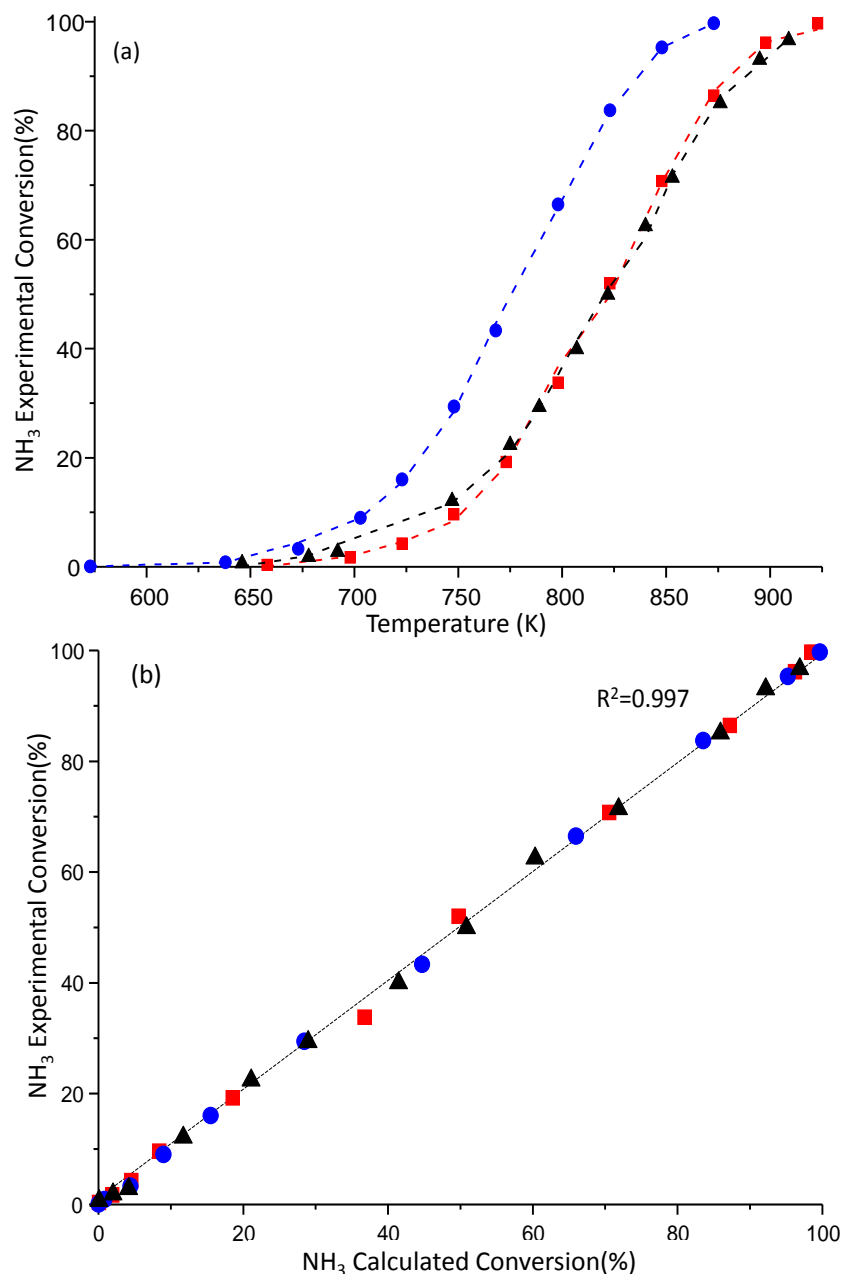
380 X_{NH_3} is the ammonia conversion, $W_{cat} / F_{NH_3}^0$ is the spatial time ($g_{cat} \text{ s/mol } NH_3$) and

382 $(-r_{NH_3})$ is given by the power-law rate expression (2). The numerical solution of eqn
383 (3), allows the calculation of the sum of the squared residuals (SSR), used as objective

384 function minimized by the Levenberg–Marquardt algorithm:

$$SSR = \min \sum_{i=1}^{i=n} (X_{NH_3}^{exp} - X_{NH_3}^{calc})^2 \quad (4)$$

385



386
 387 **Fig. 6.** (a) Dependence of NH₃ conversion with reaction temperature (symbols:
 388 experimental data; dotted line: model simulation, eqn. 2). (●) Ru(NN)/Al/M; (■)
 389 Ru(Cl)/Al/M; (▲) Ru(acac)/Al/M; (b) Parity plot of the NH₃ conversion data.

390
 391 Fig.6 a-b, shows the results of the experimental and model prediction of ammonia
 392 conversion vs. temperature data; and their excellent correlation in the parity plot (Fig. 6,
 393 b). As is in these figures the homoscedastic distribution of the errors along the entire
 394 range of conversions, indicates that power law model is an excellent approximation for
 395 the modelling of the experimental data and, according to the main hypothesis of the

396 Temkin-Pyzhev model, the rate determining step of the reaction mechanism is the
 397 associative adsorption of N-adsorbed species.

398 In the Table 2 are shown the kinetic parameters of the Temkin-Pyzhev model. The low
 399 values of the standard errors obtained in all the cases, indicate again the excellent fitting
 400 achieved, and therefore the validity of the model. Thus, the valued of the apparent
 401 activation energies presented in the Table 2 have the same tendency (i.e. Ru(NN)/Al/M
 402 < Ru(Cl)/Al/M < Ru(acac)/Al/M) that the one obtaiend by direct aplication of the
 403 Arrhenius equation to the low conversion data (Fig. 5). The good coincidence between
 404 the results obtaiend using the diferential method of the low conversion data (Figure 5)
 405 and the integral method of whole range of conversion data, eqn. 3 and Figure 6, if an
 406 additional proof of the confidence of the aproach used here.

407 Table 2: Kinetic parameters of Temkin-Pyzhev model.

Catalyst	Ru(NN)/Al ₂ O ₃ /M	Ru(acac)/Al ₂ O ₃ /M	Ru(Cl)/Al ₂ O ₃ /M
Parameter	Value	Value	Value
k ^(*)	6.99 x10 ⁻⁰⁴ ±4.22 x10 ⁻⁵	1.94 x10 ⁻⁰⁴ ±1.89 x10 ⁻⁵	1.04 x10 ⁻⁰² ± 4.29 x10 ⁻⁷
Ea(kJ/mol)	76.63±6.22	154.81±12.50	89.32±4.80
α	0.72±0.05	1.046±0.10	0.781±0.06
β	0.45±0.01	-0.278±0.02	0.439±0.03
-(α/β)	-1.57±0.06	3.75±0.12	-1.78±0.09

408 * units: mol NH₃·atm^(α+β)/g_{cat}·s
 409

410 According to the “Temkin formalism”, the ratio α/β should be between 0.4 and 0.5,
 411 however the result calculated by the fitting of the data on Figure 2 shows large
 412 differences. In fact, the kinetic orders of ammonia and hydrogen show a great variability
 413 each other, which could be associated to the different catalyst intrinsic nature, mainly
 414 the average and distribution of particle size, the Ru content, and even the shape of the
 415 particles, [33,60,61].

416 The lower activation energy and higher conversion of catalyst Ru(NN)/Al/M, compared
 417 to those prepared from the other precursors, can be attributed to its larger mean particle
 418 size (3.5 nm) which entails higher density of B₅-type sites. This behavior has been

419 explained by compensatory effects [51,62], derived from the relationship between the
420 activation energy of the rate-limiting step, and the stability of the reaction intermediates
421 on the surface of the catalyst.

422 In spite of that the Temkin-Pyzhev model provide an reasonable acknowledge of the
423 kinetic reaction mechanism, and a simple way to analyze the data, in some cases it is
424 necessary to use a more robust model, which can predict the kinetic order evolutions
425 during ammonia decomposition reaction. The kinetic orders and the apparent energies
426 of activation shown in Table 2 are an average of all the individual values which could
427 be calculated as the gas composition changes along the reactor length. In fact, we have
428 previously demonstrated [57], that the variable kinetic orders and apparent activation
429 energies frequently reported in the literature are consequence of misleading data
430 analysis, and not a consequence of the any change in the controlling step of the reaction
431 mechanism.

432

433 **4. Conclusions**

434 The results of this work show that the Ru catalyst in the form of honeycomb monoliths
435 is a robust an active catalyst for H₂ generation form ammonia decomposition, thus
436 being an enabling technology for the use of ammonia as practical H₂ storage media.

437 All the Ru-based catalysts used exhibited higher conversion in the decomposition of
438 pure ammonia than Ni-based one, despite of ca. 5-fold larger metal loading of the latter.

439 Among all the Ru-based catalysts, the highest conversion and lowest apparent activation
440 energy correspond to that prepared using ruthenium-nitrosyl-nitrate as precursor. This
441 catalyst exhibited the largest mean particle size and the highest ratio of Ru⁰/Ru_(total) in
442 reduced state after the passivation step. Thus, the highest activity of Ru prepared from

443 nitrosyl-nitrate could be explained by the higher proportion of B₅-type sites exposed,
444 which have been related to particles with the same order of size.

445 The Temkin-Pyzhev (Power-Law) kinetic model provide an reasonable acknowledge of
446 the reaction mechanism, and a simple way to analyze the data, in the whole range of
447 ammonai conversions. The values of the kinetic orders, and the apparent energies of
448 activation shown in Table 2, are valid to discriminate the intrinsic differences observed
449 between the catalysts, and to develop a complete model of the monolithic reactor.

450

451 **Aknowledgements**

452 The authors wants to aknowledge to the support of European Commission (FP7, Grant
453 agreement n° 280658). Dr Armenise wants to aknowledge specially to University of
454 Zaragoza, Institute of Carboquimica and Banco Santander Hispano to finance the
455 doctoral fellow. Finnaly the authors wants to aknowledge to Universida Politecnica
456 Salesiana to provide the economical support to attend the IMCCRE-2018.

457

458

- 460 [1] Mori D, Hirose K. Recent challenges of hydrogen storage technologies for fuel
461 cell vehicles. *International Journal of Hydrogen Energy* 2009;34:4569–74.
462 doi:<http://dx.doi.org/10.1016/j.ijhydene.2008.07.115>.
- 463 [2] Sakintuna B, Lamari-Darkrim F, Hirscher M. Metal hydride materials for solid
464 hydrogen storage: A review. *International Journal of Hydrogen Energy*
465 2007;32:1121–40. doi:<http://dx.doi.org/10.1016/j.ijhydene.2006.11.022>.
- 466 [3] Schlapbach L, Zuttel A. Hydrogen-storage materials for mobile applications.
467 *Nature* 2001;414:353–8.
- 468 [4] Holladay JD, Hu J, King DL, Wang Y. An overview of hydrogen production
469 technologies. *Catalysis Today* 2009;139:244–60.
470 doi:<http://dx.doi.org/10.1016/j.cattod.2008.08.039>.
- 471 [5] Cheng X, Shi Z, Glass N, Zhang L, Zhang J, Song D, et al. A review of PEM
472 hydrogen fuel cell contamination: Impacts, mechanisms, and mitigation. *Journal*
473 *of Power Sources* 2007;165:739–56.
474 doi:<http://dx.doi.org/10.1016/j.jpowsour.2006.12.012>.
- 475 [6] Dasireddy VDBC, Likozar B. CO_x-free hydrogen generation via decomposition
476 of ammonia over copper and zinc-based catalysts. *Fuel* 2017;196:325–35.
477 doi:<https://doi.org/10.1016/j.fuel.2017.01.117>.
- 478 [7] Schuth F, Palkovits R, Schlogl R, Su DS. Ammonia as a possible element in an
479 energy infrastructure: catalysts for ammonia decomposition. *Energy Environ Sci*
480 2012;5:6278–89. doi:10.1039/C2EE02865D.
- 481 [8] Yin SF, Xu BQ, Zhou XP, Au CT. A mini-review on ammonia decomposition
482 catalysts for on-site generation of hydrogen for fuel cell applications. *Applied*
483 *Catalysis A: General* 2004;277:1–9.
484 doi:<http://dx.doi.org/10.1016/j.apcata.2004.09.020>.
- 485 [9] Ganley JC, Seebauer EG, Masel RI. Development of a microreactor for the
486 production of hydrogen from ammonia. *Journal of Power Sources* 2004;137:53–
487 61. doi:<http://dx.doi.org/10.1016/j.jpowsour.2004.05.032>.
- 488 [10] Bradford MCJ, Fanning PE, Vannice MA. Kinetics of NH₃ Decomposition over
489 Well Dispersed Ru. *Journal of Catalysis* 1997;172:479–84.
490 doi:<http://dx.doi.org/10.1006/jcat.1997.1877>.
- 491 [11] Pyrz W, Vijay R, Binz J, Lauterbach J, Buttrey DJ. Characterization of K-
492 Promoted Ru Catalysts for Ammonia Decomposition Discovered Using High-
493 Throughput Experimentation. *Topics in Catalysis* 2008;50:180–91.
494 doi:10.1007/s11244-008-9095-y.
- 495 [12] Ju X, Liu L, Yu P, Guo J, Zhang X, He T, et al. Mesoporous Ru/MgO prepared
496 by a deposition-precipitation method as highly active catalyst for producing
497 CO_x-free hydrogen from ammonia decomposition. *Applied Catalysis B:*
498 *Environmental* 2017;211:167–75.
499 doi:<https://doi.org/10.1016/j.apcatb.2017.04.043>.
- 500 [13] Raróg-Pilecka W, Szmigiel D, Kowalczyk Z, Jodzis S, Zielinski J. Ammonia
501 decomposition over the carbon-based ruthenium catalyst promoted with barium
502 or cesium. *Journal of Catalysis* 2003;218:465–9.
503 doi:[http://dx.doi.org/10.1016/S0021-9517\(03\)00058-7](http://dx.doi.org/10.1016/S0021-9517(03)00058-7).
- 504 [14] Sørensen RZ, Klerke A, Quaade U, Jensen S, Hansen O, Christensen CH.
505 Promoted Ru on high-surface area graphite for efficient miniaturized production
506 of hydrogen from ammonia. *Catalysis Letters* 2006;112:77–81.
507 doi:10.1007/s10562-006-0167-y.

- 508 [15] Armenise S, Roldán L, Marco Y, Monzón A, García-Bordejé E. Elucidation of
509 Catalyst Support Effect for NH₃ Decomposition Using Ru Nanoparticles on
510 Nitrogen-Functionalized Carbon Nanofiber Monoliths. *The Journal of Physical
511 Chemistry C* 2012;116:26385–95. doi:10.1021/jp308985x.
- 512 [16] Chen J, Zhu ZH, Wang S, Ma Q, Rudolph V, Lu GQ. Effects of nitrogen doping
513 on the structure of carbon nanotubes (CNTs) and activity of Ru/CNTs in
514 ammonia decomposition. *Chemical Engineering Journal* 2010;156:404–10.
515 doi:http://dx.doi.org/10.1016/j.cej.2009.10.062.
- 516 [17] García-García FR, Álvarez-Rodríguez J, Rodríguez-Ramos I, Guerrero-Ruiz A.
517 The use of carbon nanotubes with and without nitrogen doping as support for
518 ruthenium catalysts in the ammonia decomposition reaction. *Carbon*
519 2010;48:267–76. doi:http://dx.doi.org/10.1016/j.carbon.2009.09.015.
- 520 [18] Zheng W, Zhang J, Zhu B, Blume R, Zhang Y, Schlichte K, et al. Structure–
521 Function Correlations for Ru/CNT in the Catalytic Decomposition of Ammonia.
522 *ChemSusChem* 2010;3:226–30. doi:10.1002/cssc.200900217.
- 523 [19] Duan X, Qian G, Zhou X, Chen D, Yuan W. MCM-41 supported CoMo
524 bimetallic catalysts for enhanced hydrogen production by ammonia
525 decomposition. *Chemical Engineering Journal* 2012;207:103–8.
526 doi:http://dx.doi.org/10.1016/j.cej.2012.05.100.
- 527 [20] Jacobsen CJH, Dahl S, Clausen BS, Bahn S, Logadottir A, Nørskov JK. Catalyst
528 Design by Interpolation in the Periodic Table: Bimetallic Ammonia Synthesis
529 Catalysts. *Journal of the American Chemical Society* 2001;123:8404–5.
530 doi:10.1021/ja010963d.
- 531 [21] Boisen A, Dahl S, Nørskov JK, Christensen CH. Why the optimal ammonia
532 synthesis catalyst is not the optimal ammonia decomposition catalyst. *Journal of
533 Catalysis* 2005;230:309–12. doi:http://dx.doi.org/10.1016/j.jcat.2004.12.013.
- 534 [22] Czekajło Ł, Lendzion-Bieluń Z. Effect of preparation conditions and promoters
535 on the structure and activity of the ammonia decomposition reaction catalyst
536 based on nanocrystalline cobalt. *Chemical Engineering Journal* 2016;289:254–
537 60. doi:http://dx.doi.org/10.1016/j.cej.2015.12.093.
- 538 [23] Srifa A, Okura K, Okanishi T, Muroyama H, Matsui T, Eguchi K. Hydrogen
539 production by ammonia decomposition over Cs-modified Co₃Mo₃N catalysts.
540 *Applied Catalysis B: Environmental* 2017;218:1–8.
541 doi:https://doi.org/10.1016/j.apcatb.2017.06.034.
- 542 [24] Christian, Mitchell M, Kim D-P, Kenis PJA. Ceramic microreactors for on-site
543 hydrogen production. *Journal of Catalysis* 2006;241:235–42.
544 doi:http://dx.doi.org/10.1016/j.jcat.2006.04.033.
- 545 [25] Deshmukh SR, Mhadeshwar AB, Vlachos DG. Microreactor Modeling for
546 Hydrogen Production from Ammonia Decomposition on Ruthenium. *Industrial &
547 Engineering Chemistry Research* 2004;43:2986–99. doi:10.1021/ie030557y.
- 548 [26] Ganley JC, Thomas FS, Seebauer EG, Masel RI. A Priori Catalytic Activity
549 Correlations: The Difficult Case of Hydrogen Production from Ammonia.
550 *Catalysis Letters* 2004;96:117–22. doi:10.1023/B:CATL.0000030108.50691.d4.
- 551 [27] Plana C, Armenise S, Monzón A, García-Bordejé E. Ni on alumina-coated
552 cordierite monoliths for in situ generation of CO-free H₂ from ammonia. *Journal
553 of Catalysis* 2010;275:228–35. doi:http://dx.doi.org/10.1016/j.jcat.2010.07.026.
- 554 [28] Löffler DG, Schmidt LD. Kinetics of NH₃ decomposition on polycrystalline Pt.
555 *Journal of Catalysis* 1976;41:440–54. doi:http://dx.doi.org/10.1016/0021-
556 9517(76)90245-1.
- 557 [29] Vajo JJ, Tsai W, Weinberg WH. Steady-state decomposition of ammonia on the

- 558 platinum(110)-(1 .times. 2) surface. The Journal of Physical Chemistry
559 1986;90:6531–5. doi:10.1021/j100282a023.
- 560 [30] Tsai W, Weinberg WH. Steady-state decomposition of ammonia on the
561 ruthenium(001) surface. The Journal of Physical Chemistry 1987;91:5302–7.
562 doi:10.1021/j100304a034.
- 563 [31] Kunsman CH. THE THERMAL DECOMPOSITION OF AMMONIA ON IRON
564 CATALYSTS. II. Journal of the American Chemical Society 1929;51:688–95.
565 doi:10.1021/ja01378a005.
- 566 [32] Tamaru K. A “new” general mechanism of ammonia synthesis and
567 decomposition on transition metals. Accounts of Chemical Research 1988;21:88–
568 94. doi:10.1021/ar00146a007.
- 569 [33] Chellappa AS, Fischer CM, Thomson WJ. Ammonia decomposition kinetics over
570 Ni-Pt/Al₂O₃ for PEM fuel cell applications. Applied Catalysis A: General
571 2002;227:231–40. doi:http://dx.doi.org/10.1016/S0926-860X(01)00941-3.
- 572 [34] Nishida T, Egawa C, Naito S, Tamaru K. Hydrogenation of nitric oxide on (0 0
573 1) and (1 1 10) surfaces of ruthenium. J Chem Soc{,} Faraday Trans 1
574 1984;80:1567–78. doi:10.1039/F19848001567.
- 575 [35] Djéga-Mariadassou G, Shin C-H, Bugli G. Tamaru’s model for ammonia
576 decomposition over titanium oxynitride. Journal of Molecular Catalysis A:
577 Chemical 1999;141:263–7. doi:http://dx.doi.org/10.1016/S1381-1169(98)00270-
578 2.
- 579 [36] D’Souza L, Regalbuto JR, Miller JT. Preparation of carbon supported cobalt by
580 electrostatic adsorption of [Co(NH₃)₆]Cl₃. Journal of Catalysis 2008;254:157–
581 69. doi:http://dx.doi.org/10.1016/j.jcat.2007.12.007.
- 582 [37] Nijhuis TA, Beers AEW, Vergunst T, Hoek I, Kapteijn F, Moulijn JA.
583 Preparation of monolithic catalysts. Catalysis Reviews 2001;43:345–80.
584 doi:10.1081/CR-120001807.
- 585 [38] García-Bordejé E, Kvande I, Chen D, Rønning M. Synthesis of composite
586 materials of carbon nanofibres and ceramic monoliths with uniform and tuneable
587 nanofibre layer thickness. Carbon 2007;45:1828–38.
588 doi:http://dx.doi.org/10.1016/j.carbon.2007.04.026.
- 589 [39] Chan HYH, Takoudis CG, Weaver MJ. High-Pressure Oxidation of Ruthenium
590 as Probed by Surface-Enhanced Raman and X-Ray Photoelectron Spectroscopies.
591 Journal of Catalysis 1997;172:336–45.
592 doi:http://dx.doi.org/10.1006/jcat.1997.1841.
- 593 [40] Elmasides C, Kondarides DI, Grünert W, Verykios XE. XPS and FTIR Study of
594 Ru/Al₂O₃ and Ru/TiO₂ Catalysts: Reduction Characteristics and Interaction with
595 a Methane–Oxygen Mixture. The Journal of Physical Chemistry B
596 1999;103:5227–39. doi:10.1021/jp9842291.
- 597 [41] Mazziari V, Coloma-Pascual F, Arcoya A, L’Argentièrè PC, Fí́goli NS.
598 XPS, FTIR and TPR characterization of Ru/Al₂O₃ catalysts. Applied Surface
599 Science 2003;210:222–30. doi:http://dx.doi.org/10.1016/S0169-4332(03)00146-
600 6.
- 601 [42] Okal J, Zawadzki M, Tylus W. Microstructure characterization and propane
602 oxidation over supported Ru nanoparticles synthesized by the microwave-polyol
603 method. Applied Catalysis B: Environmental 2011;101:548–59.
604 doi:http://dx.doi.org/10.1016/j.apcatb.2010.10.028.
- 605 [43] Rolison DR, Hagans PL, Swider KE, Long JW. Role of Hydrous Ruthenium
606 Oxide in Pt–Ru Direct Methanol Fuel Cell Anode Electrocatalysts: The
607 Importance of Mixed Electron/Proton Conductivity. Langmuir 1999;15:774–9.

- doi:10.1021/la9807863.
- [44] Zhong Z, Aika K. Effect of ruthenium precursor on hydrogen-treated active carbon supported ruthenium catalysts for ammonia synthesis. *Inorganica Chimica Acta* 1998;280:183–8. doi:http://dx.doi.org/10.1016/S0020-1693(98)00202-3.
- [45] Maroto-Valiente A, Cerro-Alarcón M, Guerrero-Ruiz A, Rodríguez-Ramos I. Effect of the metal precursor on the surface site distribution of Al₂O₃-supported Ru catalysts: catalytic effects on the n-butane/H₂ test. *Applied Catalysis A: General* 2005;283:23–32. doi:http://dx.doi.org/10.1016/j.apcata.2004.12.047.
- [46] Plana C, Armenise S, Monzón A, García-Bordejé E. Ni on alumina-coated cordierite monoliths for in situ generation of CO-free H₂ from ammonia. *Journal of Catalysis* 2010;275. doi:10.1016/j.jcat.2010.07.026.
- [47] Jacobsen CJH, Dahl S, Hansen PL, Törnqvist E, Jensen L, Topsøe H, et al. Structure sensitivity of supported ruthenium catalysts for ammonia synthesis. *Journal of Molecular Catalysis A: Chemical* 2000;163:19–26. doi:http://dx.doi.org/10.1016/S1381-1169(00)00396-4.
- [48] Choudhary T V, Sivadinarayana C, Goodman DW. Catalytic ammonia decomposition: CO_x-free hydrogen production for fuel cell applications. *Catalysis Letters* 2001;72:197–201. doi:10.1023/A:1009023825549.
- [49] García-García FR, Guerrero-Ruiz A, Rodríguez-Ramos I. Role of B5-Type Sites in Ru Catalysts used for the NH₃ Decomposition Reaction. *Topics in Catalysis* 2009;52:758–64. doi:10.1007/s11244-009-9203-7.
- [50] Karim AM, Prasad V, Mpourmpakis G, Lonergan WW, Frenkel AI, Chen JG, et al. Correlating Particle Size and Shape of Supported Ru/γ-Al₂O₃ Catalysts with NH₃ Decomposition Activity. *Journal of the American Chemical Society* 2009;131:12230–9. doi:10.1021/ja902587k.
- [51] Zheng W, Zhang J, Xu H, Li W. NH₃ Decomposition Kinetics on Supported Ru Clusters: Morphology and Particle Size Effect. *Catalysis Letters* 2007;119:311–8. doi:10.1007/s10562-007-9237-z.
- [52] Liu H. AMMONIA SYNTHESIS CATALYSTS: Innovation and Practice. Cao Xiangh. Beijing: World Scientific Publishing Co. Pte. Ltd; 2013.
- [53] Weisz PB, Prater CD. Interpretation of Measurements in Experimental Catalysis. In: Frankenburg WG, Komarewsky VI, Rideal EK, editors. vol. 6, Academic Press; 1954, p. 143–96. doi:https://doi.org/10.1016/S0360-0564(08)60390-9.
- [54] Holmgren A, Andersson B. Mass transfer in monolith catalysts—CO oxidation experiments and simulations. *Chemical Engineering Science* 1998;53:2285–98. doi:https://doi.org/10.1016/S0009-2509(98)00080-3.
- [55] Mears DE. Diagnostic criteria for heat transport limitations in fixed bed reactors. *Journal of Catalysis* 1971;20:127–31. doi:https://doi.org/10.1016/0021-9517(71)90073-X.
- [56] Restivo J, Órfão JJM, Pereira MFR, Vanhaecke E, Rønning M, Iouranova T, et al. Catalytic ozonation of oxalic acid using carbon nanofibres on macrostructured supports. *Water Science and Technology* 2012;65. doi:10.2166/wst.2012.882.
- [57] Armenise S, García-Bordejé E, Valverde JL, Romeo E, Monzón A. A Langmuir-Hinshelwood approach to the kinetic modelling of catalytic ammonia decomposition in an integral reactor. *Physical Chemistry Chemical Physics* 2013;15. doi:10.1039/c3cp50715g.
- [58] Emmett PH, Kummer JT. Kinetics of Ammonia Synthesis. *Industrial & Engineering Chemistry* 1943;35:677–83. doi:10.1021/ie50402a012.
- [59] M. Temkin VP. Kinetics of the synthesis of ammonia on promoted iron catalysts. *Acta Physicochim URSS*, 1939;12:327–56.

- 658 [60] Bell TE, Torrente-Murciano L. H₂ Production via Ammonia Decomposition
659 Using Non-Noble Metal Catalysts: A Review. *Topics in Catalysis* 2016;59:1438–
660 57. doi:10.1007/s11244-016-0653-4.
- 661 [61] Zhang J, Xu H, Li W. Kinetic study of NH₃ decomposition over Ni
662 nanoparticles: The role of La promoter, structure sensitivity and compensation
663 effect. *Applied Catalysis A: General* 2005;296:257–67.
664 doi:<https://doi.org/10.1016/j.apcata.2005.08.046>.
- 665 [62] Bligaard T, Honkala K, Logadottir A, Nørskov JK, Dahl S, Jacobsen CJH. On the
666 Compensation Effect in Heterogeneous Catalysis. *The Journal of Physical*
667 *Chemistry B* 2003;107:9325–31. doi:10.1021/jp034447g.
668